Hydrogen-mediated quenching of strain-induced surface roughening during gas-source molecular beam epitaxy of fully-coherent $Si_{0.7}Ge_{0.3}$ layers on Si(001)

T. Spila, P. Desjardins,[a] A. Vailionis, H. Kim, N. Taylor, D. G. Cahill, and J. E. Greene[b]
Department of Materials Science and the Frederick Seitz Materials Research Laboratory, University of Illinois, 104 South Goodwin Avenue, Urbana, Illinois 61801

S. Guillon and R. A. Masut
Groupe de Recherche en Physique et Technologie des Couches Minces and Département de Génie Physique, École Polytechnique de Montréal, P.O. Box 6079, Station Centre-Ville, Montréal, Québec H3C 3A7, Canada

(Received 1 October 2001; accepted for publication 4 December 2001)

Fully-coherent $Si_{0.7}Ge_{0.3}$ layers were deposited on Si(001) by gas-source molecular beam epitaxy (GS-MBE) from Ge_2H_6/Si_2H_6 mixtures in order to probe the effect of steady-state hydrogen coverages θ_H on surface morphological evolution during the growth of compressively strained films. The layers are grown as a function of thickness t at temperatures, $T_s = 450-550\,^\circ C$, for which strain-induced roughening is observed during solid-source MBE (SS-MBE) and deposition from hyperthermal beams. With GS-MBE, we obtain three-dimensional (3D) strain-induced growth mounds in samples deposited at $T_s = 550\,^\circ C$ for which θ_H is small, 0.11 monolayer (ML). However, mound formation is dramatically suppressed at $500\,^\circ C$ ($\theta_H = 0.26$ ML) and completely eliminated at $450\,^\circ C$ ($\theta_H = 0.52$ ML). We attribute these large differences in surface morphological evolution primarily to $\theta_H(T_s)$-induced effects on film growth rates R, adatom diffusion rates D_s, and ascending step-crossing probabilities. GS-MBE $Si_{0.7}Ge_{0.3}(001)$ growth at $450\,^\circ C$ remains two dimensional, with a surface width $\langle w \rangle < 0.15$ nm, at all film thicknesses $t = 11-80$ nm, since both R and the rate of mass transport across ascending steps are low. Raising T_s to $500\,^\circ C$ increases R faster than D_s leading to shorter mean surface diffusion lengths and the formation of extremely shallow, rounded growth mounds for which $\langle w \rangle$ remains essentially constant at $\simeq 0.2$ nm while the in-plane coherence length $\langle d \rangle$ increases from $\simeq 70$ nm at $t = 14$ nm to 162 nm with $t = 75$ nm. The low ascending step crossing probability at $500\,^\circ C$ results in mounds that spread laterally, rather than vertically, due to preferential attachment at the mound edges. At $T_s = 550\,^\circ C$, the ascending step crossing probability increases due to both higher thermal activation and lower hydrogen coverages. $\langle w \rangle(t)$ increases by more than a factor of 10, from 0.13 nm at $t = 15$ nm to 1.9 nm at $t = 105$ nm, while the in-plane coherence length $\langle d \rangle$ remains constant at $\simeq 85$ nm. This leads, under the strain driving force, to the formation of self-organized 3D {105}-faceted pyramids at $550\,^\circ C$ which are very similar to those observed during SS-MBE. *© 2002 American Institute of Physics.* [DOI: 10.1063/1.1448680]

I. INTRODUCTION

The development of a detailed atomic-level understanding of surface morphological evolution during heteroepitaxial growth is of intense current interest for both scientific and technological reasons. Predicting and minimizing surface roughening is required for the fabrication, through band gap engineering of high-frequency planar $Si_{1-x}Ge_x$-based heterostructure devices with enhanced hole[1] and electron[2] mobilities while controlled and reproducible roughening forms the basis for novel devices based upon self-organized quantum dots and wires.[3]

Relaxation via strain-induced roughening is thermodynamically favorable in strained layers when the energy increase associated with the higher surface area is overcome by the decrease in the total strain energy of the system. Partial strain relaxation is provided through lateral expansion (compression) of the vertical planes in the mounds (valleys). Thus, there is a critical surface perturbation wavelength for a given materials system.[4] Tersoff and LeGoues[5] showed that the activation energy for strain-induced roughening decreases rapidly with an increase in misfit strain ε, varying as ε^{-4}. In contrast, the activation energy for dislocation nucleation and multiplication, a competing strain relaxation mechanism, varies much more slowly with layer strain yielding an ε^{-1} dependence. Below a temperature-dependent critical layer/substrate misfit, the system strain energy is reduced by misfit dislocation formation prior to significant surface roughening. The temperature at which strain-induced

[a]Present address: Groupe de Recherche en Physique et Technologie des Couches Minces, Département de génie physique, École Polytechnique de Montréal, P.O. Box 6079, Station Center-Ville, Montréal, Québec H3C 3A7, Canada.
[b]Electronic mail: greene@mrlxp2.mrl.uiuc.edu

Downloaded 07 Nov 2002 to 130.126.102.122. Redistribution subject to AIP license or copyright, see http://ojps.aip.org/japo/japcr.jsp

roughening becomes favored over misfit-dislocation nucleation decreases with an increase in misfit.[5,6]

During the initial growth of $Si_{0.7}Ge_{0.3}$ on Si(001), with a misfit of 1.2%, by solid-source molecular beam epitaxy (SS-MBE), strain-induced roughening leading to three-dimensional (3D) mound formation has been shown to be the dominant mechanism for strain relaxation at temperatures $T_s \geq 400\,°C$.[7,8] Similar results, with slightly higher temperatures, $T_s > 440\,°C$, were reported for $Si_{0.7}Ge_{0.3}$/Si(001) growth from hyperthermal beams.[9]

Recently, gas source-molecular beam epitaxy (GS-MBE) and ultrahigh vacuum chemical vapor deposition (UHV-CVD) have been shown to offer several advantages over solid-source MBE for the growth of Si (Ref. 10) and $Si_{1-x}Ge_x$.[11,12] These include the elimination of hot crucibles, higher sample throughput, better conformal coverage, better lateral uniformity, and the potential for selective epitaxy on patterned substrates. In addition, the presence of a steady-state H coverage θ_H during $Si_{1-x}Ge_x(001)$ growth form hydride precursors has been shown to decrease the rate of Ge segregation.[13] θ_H can also be expected to have a significant effect on strain-induced surface roughening kinetics through changes in growth rates and adatom ascending step crossing probabilities.

In the present investigation, we use scanning tunneling microscopy (STM), atomic force microscopy (AFM), and x-ray reflectivity (XRR) to follow the effects of varying θ_H on surface morphological evolution during $Si_{0.7}Ge_{0.3}$ growth on Si(001) by GS-MBE at temperatures $T_s = 450$, 500, and 550 °C and thicknesses t up to the critical value for misfit dislocations. The *in situ* STM and *ex situ* AFM surface roughening results are quantified in terms of the height–difference and height–height correlation functions to determine surface widths $\langle w \rangle$ and in-plane coherence lengths $\langle d \rangle$. In contrast to SS-MBE, we find that GS-MBE $Si_{0.7}Ge_{0.3}(001)$ alloys grown at $T_s = 450\,°C$, for which $\theta_H = 0.52$ monolayer (ML), are smooth ($\langle w \rangle < 0.15$ nm) at all thicknesses ($t = 11$–80 nm). Three-dimensional roughening is suppressed even at $T_s = 500\,°C$, where $\theta_H = 0.26$ ML: layer surfaces exhibit extremely shallow, rounded growth mounds with $\langle w \rangle(t)$ remaining essentially constant at $\simeq 0.2$ nm. The aspect ratio $\langle w \rangle / \langle d \rangle$ of the $T_s = 500\,°C$ mounds decreases by a factor of 2 with an increase in t between 14 and 75 nm due to a corresponding increase in $\langle d \rangle$. Surface morphological evolution in GS-MBE $Si_{0.7}Ge_{0.3}$ layers grown at 550 °C ($\theta_H = 0.11$ ML) is, due to low steady-state hydrogen coverages, more closely related to that of SS-MBE layers. The films exhibit surface features for which $\langle w \rangle / \langle d \rangle$ increases with t (15–105 nm) by more than a factor of 10 due to increases in $\langle w \rangle$ while $\langle d \rangle$ remains constant. The striking differences in surface morphological evolution observed during $Si_{1-x}Ge_x(001)$ GS-MBE over a relatively narrow growth temperature range, where 3D surface roughening is observed throughout during SS-MBE, suggests that θ_H plays an important role in mediating the kinetics of strain-induced roughening through changes in film growth rates as well as adatom mean-free paths and step-crossing probabilities.

TABLE I. $Si_{0.7}Ge_{0.3}(001)$ GS-MBE growth rate R and Ge and H steady-state surface coverages (θ_{Ge} and θ_H) as a function of deposition temperature T_s.

T_s (°C)	R (nm min^{-1})	θ_{Ge} (ML)	θ_H (ML)
450	1.02	0.79	0.52
500	7.84	0.82	0.26
550	13.5	0.86	0.11

II. EXPERIMENTAL PROCEDURE

All $Si_{0.7}Ge_{0.3}(001)$ layers were grown in a multichamber UHV system, described in detail in Ref. 14, with a base pressure of 5×10^{-11} Torr. The system is equipped with provisions for temperature programmed desorption (TPD), reflection high-energy electron diffraction (RHEED), low-energy electron diffraction (LEED), electron energy loss spectroscopy (EELS), Auger electron spectroscopy (AES), and STM. The film growth experiments were carried out using Si_2H_6 and Ge_2H_6 precursor fluxes of 2.1×10^{16} and 1.3–1.5×10^{15} cm^{-2} s^{-1}, respectively. The Ge_2H_6/Si_2H_6 flux ratio was chosen to maintain the composition of all layers at $x = 0.3$, irrespective of T_s. During deposition, the Si_2H_6 and Ge_2H_6 molecular beams are delivered to the substrate through individual directed tubular dosers. Layer growth rates R were determined to be 1.02, 7.85, and 13.5 nm min^{-1} for $T_s = 450$, 500, and 550 °C, respectively (Table I).

The substrates are 0.5-mm-thick n-type Si(001) wafers (1–2×10^{14} cm^{-3}) with a miscut of $\simeq 0.1°$ in the $\langle 110 \rangle$ direction. Substrate degreasing and cleaning, including wet-chemical oxidation/etch cycles, an ultraviolet ozone treatment, and UHV degassing and oxide desorption, are described in Ref. 15. RHEED patterns of substrates subjected to this procedure are 2×1 with sharp Kikuchi lines. No residual C or O is detected by AES. Si(001) buffer layers, 300 nm thick, were deposited at $T_s = 800\,°C$ prior to growth of the $Si_{0.7}Ge_{0.3}$ alloy layers at $T_s = 450$–550 °C. The Si_2H_6 flux was uninterrupted while decreasing T_s in order to minimize surface contamination.

Deposited layer thicknesses t and compositions x were determined using a combination of Rutherford backscattering spectroscopy (RBS), XRR, and high-resolution x-ray diffraction (HR-XRD) analyses. The reported values for t and x are accurate to within ± 0.5 nm and $\pm 3 \times 10^{-3}$, respectively, and the results show that the variation in layer composition is less than 2×10^{-2}. The RBS measurements were carried out using 2 MeV He^+ ions, and the data analyzed with the RUMP simulation program.[16] The XRR scans, which were fit based upon the Fresnel reflectivity formulation of Parratt,[17] were obtained using a Bede HR-XRD system operated with a Cu $K\alpha_1$ monochromatic beam (0.154 0597 nm).

HR-XRD measurements were performed by a Philips diffractometer with Cu $K\alpha_1$ radiation from a four-crystal Ge(220) monochromator which provides an angular divergence of < 12 arcsec with a wavelength spread of 7×10^{-5}. ω–2θ overview scans (ω is the angle of incidence and θ is the Bragg diffraction angle) were obtained with a

Downloaded 07 Nov 2002 to 130.126.102.122. Redistribution subject to AIP license or copyright, see http://ojps.aip.org/japo/japcr.jsp

detector acceptance angle of $\simeq 2°$. An additional two-crystal Ge(220) analyzer was placed between the sample and the detector to obtain high-resolution (detector acceptance angle $\simeq 12$ arcsec) scans and high-resolution reciprocal lattice maps (HR-RLMs) about both symmetric and asymmetric reflections. HR-RLMs were generated from successive ω–2θ scans starting at different initial values of ω.

$Si_{0.7}Ge_{0.3}(001)$ surface morphological evolution was investigated as a function of the layer thickness and growth temperature using *in situ* STM and *ex situ* contact-mode AFM. STM measurements were performed using a Park Scientific instrument operated with a constant tunneling current of 0.75–1.28 nA and a tip bias of 2.49–2.75 V. AFM analyses were carried out in air using Digital Instruments Nanoscope II and Multimode microscopes with oxide-sharpened Si_3N_4 tips having radii of 5–40 nm. The images were linearly planarized to remove sample tilt effects during the measurements. Additional line-by-line leveling was performed on the smoothest samples to remove low frequency vibrational noise.

Height-difference, $G(\rho)=\langle|h_j-h_i|^2\rangle$, and height-height, $H(\rho)=\langle h_i h_j\rangle$, correlation functions, where h_i and h_j are surface heights at positions i and j separated by a distance ρ and the angled brackets correspond to averages over the measured surface, were calculated from the STM and AFM images. The dominant in-plane length scale $\langle d\rangle$ is determined from the first maximum in $H(\rho)$, while the surface width $\langle w\rangle$, which is equivalent to the root-mean-square (rms) roughness, is the average of the w values calculated at each ρ using the relation $2w^2=G(\rho)+2H(\rho)$. Two-dimensional slope histograms were constructed from the vector normals to the surface at all points in the AFM images and are plotted with increasing surface angle from the center of the image.

III. EXPERIMENTAL RESULTS

We report results for surface morphological evolution as a function of film thickness t and growth temperature T_s during GS-MBE of fully coherent $Si_{0.7}Ge_{0.3}$ layers on Si(001). Steady-state H and Ge surface coverages (θ_H and θ_{Ge}) during growth were determined using isotopically tagged D_2 TPD measurements following the procedure described in Refs. 13 and 18 and are listed with film growth rates R in Table I. While θ_{Ge} remains relatively constant, increasing slightly from 0.79 to 0.86 ML as T_s increases from 450 to 550 °C, θ_H decreases rapidly from 0.52 ML at 450 °C to 0.26 ML at 500 °C to 0.11 ML at 550 °C. These factors, as discussed below, lead to R varying from 1.02 nm min^{-1} at 450 °C to 7.84 nm min^{-1} at 500 °C to 13.5 nm min^{-1} at 550 °C.

XRR was used to determine layer thicknesses as well as to provide a quantitative measure of layer and interface rms roughness for features with an in-plane length scale less than the x-ray coherence length which, as determined from the incident beam divergence, is $\simeq 2.5$ μm. Figures 1(a)–1(c) show typical low-angle θ–2θ reflectivity scans obtained from $Si_{0.7}Ge_{0.3}(001)$ layers grown at $T_s=450$, 500, and 550 °C, respectively. The reflectivity values I_R are multiplied by θ^4

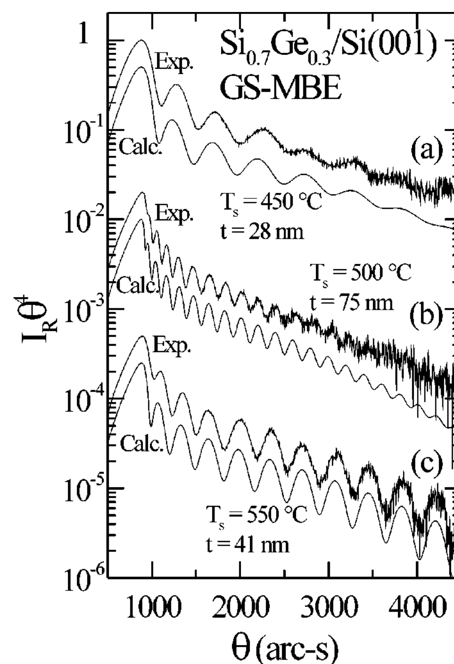

FIG. 1. XRR curves of $Si_{0.7}Ge_{0.3}$ layers grown on Si(001) to thicknesses t at temperatures T_s. (a) $t=28$ nm, $T_s=450$ °C; (b) $t=75$ nm, $T_s=500$ °C; and (c) $t=41$ nm, $T_s=550$ °C. Calculated curves are shown for comparison. The curves are shifted vertically for clarity.

to account for the angular dependence of the intensity decrease from a perfectly flat surface.[19] Thus, the rate of decrease in $I_R\theta^4$ with an increase in θ is directly correlated to the surface roughness, while the interface roughness can be determined from the damping of the intensity oscillations. The layer thickness is inversely proportional to the oscillation period.

Measured XRR scans were fit to theoretical curves calculated from the recursive theory of Parratt based upon the Fresnel reflectivity formalism.[17] The Si substrates and $Si_{0.7}Ge_{0.3}$ overlayers are assumed to have a constant electron density, and the reflectivity at the top of each successive lamella is expressed in terms of its value at the top of the previous layer.[17] Roughnesses at the top surface and at the substrate/layer interface are modeled as Gaussian distributions of the electron density about the interface position and are directly incorporated into the Fresnel coefficients. The measured and calculated curves in Fig. 1 are in very good agreement with respect to the angular position and intensity for all peaks, including the overall decay due to surface roughness.

From the results in Fig. 1, we obtain layer thicknesses together with surface and interfacial roughnesses. The thickness of the $T_s=450$ °C $Si_{0.7}Ge_{0.3}(001)$ layer shown in Fig. 1(a) is 28 nm with surface and interface roughnesses of 0.8 and 1.5 nm, respectively. Corresponding results obtained from Fig. 1(b) for the 500 °C layer are 75, 1.0, and 1.5 nm. The damping of the oscillations at high θ values is primarily due to interfacial roughness. Analysis of the XRR curves in Fig. 1(c), obtained from a $Si_{0.7}Ge_{0.3}(001)$ alloy grown at $T_s=550$ °C, shows that the layer thickness is 41 nm with a surface roughness, 0.9 nm, between that of the 450 °C

Downloaded 07 Nov 2002 to 130.126.102.122. Redistribution subject to AIP license or copyright, see http://ojps.aip.org/japo/japcr.jsp

TABLE II. XRR and HR-XRD results for all coherent GS-MBE $Si_{0.7}Ge_{0.3}(001)$ layers as a function of deposition temperature T_s. t_{XRR}, $\langle w\rangle_i$, and $\langle w\rangle_s$ are the layer thicknesses, interface roughnesses, and surface roughnesses obtained from analysis of XRR scans; x_{004} and x_{113} are the $Si_{1-x}Ge_x(001)$ Ge fractions determined from 004 HR-XRD scans and 113 HR-RLMs, respectively.

	XRR			004 XRD	HR-RLM
T_s (°C)	t_{XRR} (nm)	$\langle w\rangle_i$ (nm)	$\langle w\rangle_s$ (nm)	x_{004}	x_{113}
450	11	0.7	0.8	0.291	n/a
450	28	1.5	0.8	0.310	0.304
450	51	1.3	0.7	0.318	0.315
450	67	3.4	0.7	0.324	0.317
450	80	3.4	0.7	0.329	0.326
500	13	0.1	0.8	0.332	n/a
500	24	0.5	1.2	0.319	0.330
500	59	1.5	1.0	0.319	0.311
500	75	1.5	1.0	0.316	0.315
550	28	0.5	0.8	0.312	0.327
550	41	0.75	0.9	0.319	0.305
550	70	0.75	1.0	0.309	0.296
550	105	1.3	1.9	0.323	0.320

sample in Fig. 1(a) and the 500 °C sample in Fig. 1(b). The latter follows from the fact that the curve in Fig. 1(c) has a slope which is between those of the other two samples. However, the XRR curve in Fig. 1(c) exhibits less damping at higher diffraction angles indicating that the 550 °C layer has a smaller interfacial width, 0.75 nm.

The complete set of XRR results is presented in Table II and shows that the substrate/layer interfacial roughness increases with t at all T_s values. Except for the $t=105$ nm sample grown at $T_s=550$ °C for which $\langle w\rangle$ is 1.9 nm, all XRR surface roughnesses are $\simeq 1.0\pm 0.3$ nm. This value, corresponding to the rms roughness measured over areas defined by the x-ray coherence length ($\simeq 2.5$ μm), reflects the long wavelength undulations, $\simeq 1$ μm, which are formed during buffer layer growth at $T_s=800$ °C and are observed in large scale (14×14 μm^2) AFM images. The XRR layer thicknesses are in very good agreement with the growth rate calibrations, obtained by surface profilometry, versus T_s.

Typical HR-XRD ω–2θ scans through the 004 Bragg peak are shown in Fig. 2 for the thickest, fully coherent $Si_{0.7}Ge_{0.3}(001)$ layers grown at each temperature. The scans from the $T_s=450$ and 500 °C samples [Figs. 2(a) and 2(b)] exhibit sharp layer peaks located $-0.828°$ and $-0.805°$ from their respective substrate peaks. Finite-thickness interference fringes are clearly visible in both scans, indicating that the alloy layers are of high structural quality with laterally uniform buffer layer/film interfaces.

Simulated HR-XRD scans, based on the fully dynamical formalism of Takagi[20] and of Taupin[21] are shown in Fig. 2 for comparison. The simulations were carried out assuming perfectly abrupt and coherent interfaces, in agreement with HR-RLM results below, with linearly interpolated elastic constants. The measured and simulated curves in Figs. 2(a) and 2(b) are in excellent agreement with respect to the angular position and relative intensities of both the diffraction

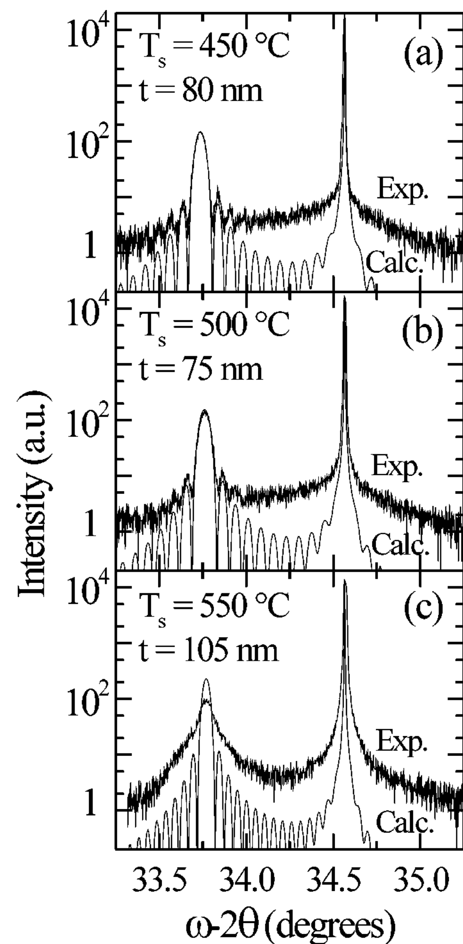

FIG. 2. ω–2θ HR-XRD scans through the Si(004) Bragg peak in $Si_{0.7}Ge_{0.3}$ layers grown on Si(001): (a) $t=80$ nm, $T_s=450$ °C; (b) $t=75$ nm, $T_s=500$ °C; and (c) $t=105$ nm, $T_s=550$ °C. Fully dynamical simulations of the HR-XRD ω–2θ scans are shown for comparison.

peaks and the interference fringes. From the scans and simulations, the Ge compositions of the 450 and 500 °C layers were determined to be 0.329 and 0.316, respectively, while the film thickness values deduced from the period of the interference fringes are in very good agreement with XRR results.

In contrast to the HR-XRD data from the lower-temperature samples, the scan of the sample grown at $T_s=550$ °C [Fig. 2(c)] exhibits broadening in the lower intensity regions of both the substrate and layer peaks and no thickness fringes. Since the HR-RLMs presented below show that the film is fully coherent with its substrate, we attribute the loss of interference fringes to increased surface roughness, consistent with XRR and AFM (see below) measurements. The Ge fraction determined from the position of the 004 alloy peak at $-0.796°$ is 0.323. Film compositions determined from the 004 scans are listed in Table II.

HR-RLMs around asymmetric 113 reflections are shown in Fig. 3 for the three samples presented in Fig. 2. Diffracted intensities are plotted as isointensity contours as a function of the reciprocal lattice vectors $k_\parallel$ parallel and $k_\perp$ perpendicular to the surface. In all cases, the substrate and film scattering distributions are essentially perfectly aligned (to within 1×10^{-5}) in the $k_\parallel$ direction showing that the layers

Downloaded 07 Nov 2002 to 130.126.102.122. Redistribution subject to AIP license or copyright, see http://ojps.aip.org/japo/japcr.jsp

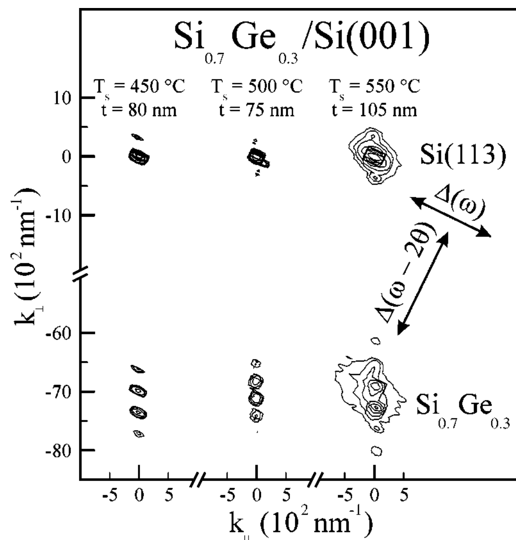

FIG. 3. HR-RLMs near the 113 Bragg peak in $Si_{0.7}Ge_{0.3}$ layers grown on Si(001): (a) $t=80$ nm, $T_s=450\,°C$; (b) $t=75$ nm, $T_s=500\,°C$; and (c) $t=105$ nm, $T_s=550\,°C$.

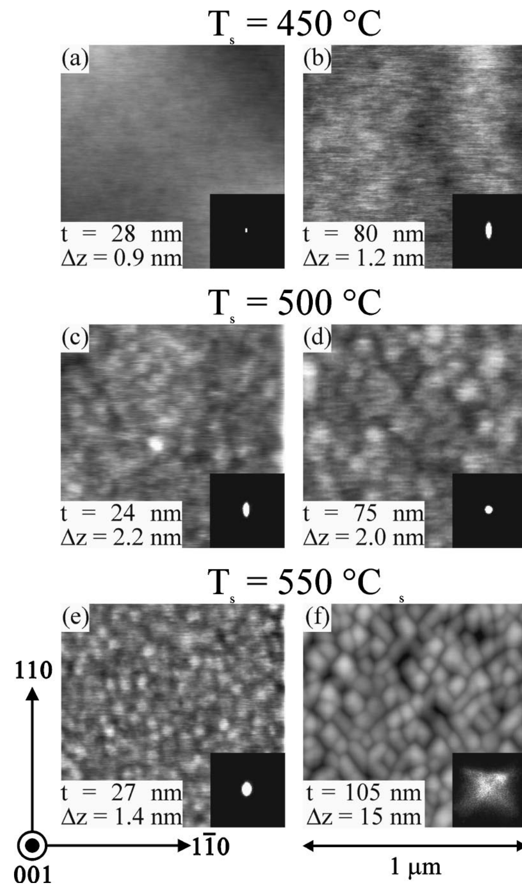

FIG. 4. AFM images of (a) $t=28$- and (b) 80-nm-thick $Si_{0.7}Ge_{0.3}(001)$ layers grown at $T_s=450\,°C$; (c) $t=24$- and (d) 75-nm-thick layers grown at $T_s=500\,°C$; and (e) $t=27$- and (f) 105-nm-thick layers grown at $T_s=550\,°C$. Δz is the black-to-white gray scale value. The insets show two-dimensional slope histograms that range over $\pm 12°$ in the x and y directions.

are fully coherent with their substrates. The diffraction contours for the $T_s=450$ and $500\,°C$ films are nearly symmetric with no broadening in the ω or $k_\parallel$ directions, an indication of high crystalline quality and low mosaicity. Thickness fringes are also visible as periodic intensity distributions along the growth direction. The positions of the 113 layer peaks correspond to Ge fractions of 0.326 and 0.315 for the 450 and $500\,°C$ films, respectively, in excellent agreement with values deduced from the 004 ω–2θ HR-XRD scans.

Thickness fringes are also visible in the HR-RLM from the $T_s=550\,°C$ sample. However, broadening in the ω direction is observed in the low intensity regions of both the substrate and the layer peaks, suggesting increased surface roughness and mosaicity compared to in the 450 and $500\,°C$ samples. The Ge fraction in the $550\,°C$ alloy, obtained from the HR-RLM in Fig. 3(c), is 0.320, also in agreement with HR-XRD results. Table II summarizes the HR-RLM results as a function of t and T_s for all layers.

Typical $1\times 1\,\mu m^2$ AFM images and corresponding two-dimensional (2D) slope histograms from $Si_{0.7}Ge_{0.3}(001)$ alloys are shown in Fig. 4. The black-to-white gray scale values Δz where chosen to be four times the standard deviation of the height distribution around the average value and are therefore approximately proportional to the surface width $\langle w\rangle$. Layers grown at $450\,°C$ show no evidence of surface mounding or roughening over the entire thickness range measured; $\langle w\rangle$ remains less than 0.15 nm. Example AFM images are presented in Figs. 4(a) and 4(b), respectively, for 28- and 80-nm-thick $Si_{0.7}Ge_{0.3}(001)$ layers. The contrast observed at the upper left and lower right corners of the image in Fig. 4(a) arises from long-wavelength undulations in the $T_s=800\,°C$ buffer layer. The contrast in Fig. 4(b) is primarily due to vibrational noise.

The intensity distributions in the 2D slope histograms in Figs. 4(a) and 4(b) exhibit Gaussian shapes, centered at the origin with no intensity beyond $1°$ and $2.5°$, respectively. This indicates that the local surface slopes are extremely shallow. The vertical elongation in the intensity distribution in Fig. 4(b) is an artifact due to the low layer roughness and the line-by-line leveling procedure performed to remove low-frequency noise.

The preceding AFM results are consistent with the $100\times 100\,nm^2$ *in situ* STM image in Fig. 5(a) of a 31-nm-thick layer grown at $450\,°C$. The image shows the surface to be flat, with 2D islands on terraces with average sizes of $\simeq 20$ nm. The absence of 3D islands combined with the fact that $\langle w\rangle$ remains constant as a function of t provides evidence that growth at $T_s=450\,°C$ proceeds in a 2D mode.

AFM images from the thinnest $500\,°C$ layers examined ($t=14$ nm) show that surface roughness is dominated by small rounded growth mounds. As t increases, the growth mounds remain round, but coarsen and become better defined. Typical images are presented in Figs. 4(c) and 4(d) for samples with thicknesses of 24 and 75 nm. Mound coarsening in these samples occurs without significant changes in the average mound height. $\langle w\rangle$, $\langle d\rangle$, and the aspect ratio $\langle w\rangle/\langle d\rangle$ are plotted as a function of layer thickness in Fig. 6. The results show that $\langle w\rangle$ remains essentially constant with thickness [Fig. 6(a)] for alloy layers grown at $T_s=500\,°C$, varying from 0.18 nm at $t=14$ nm to 0.20 nm with $t=75$ nm, whereas $\langle d\rangle$ increases steadily from $\simeq 70$ to 162

Downloaded 07 Nov 2002 to 130.126.102.122. Redistribution subject to AIP license or copyright, see http://ojps.aip.org/japo/japcr.jsp

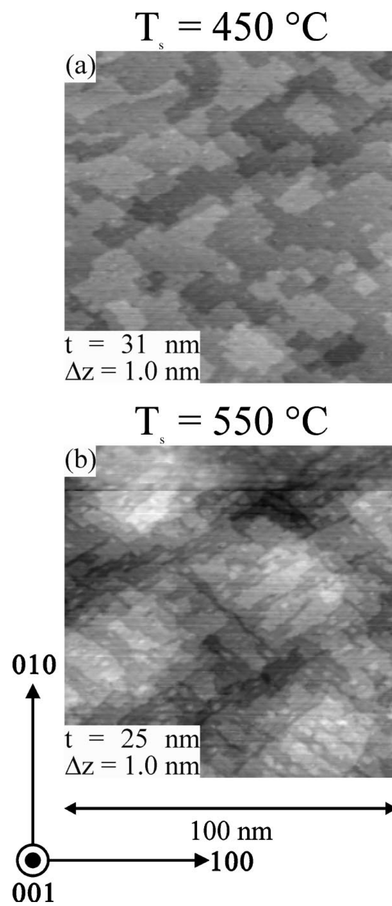

FIG. 5. STM images of $Si_{0.7}Ge_{0.3}$ layers grown on Si(001): (a) $t=31$ nm, $T_s=450\,°C$ and (b) $t=25$ nm, $T_s=550\,°C$. Δz is the black-to-white gray scale value. The tunneling current and tip voltages were (a) 1.03 nA and 2.49 V and (b) 0.75 nA and 2.75 V, respectively.

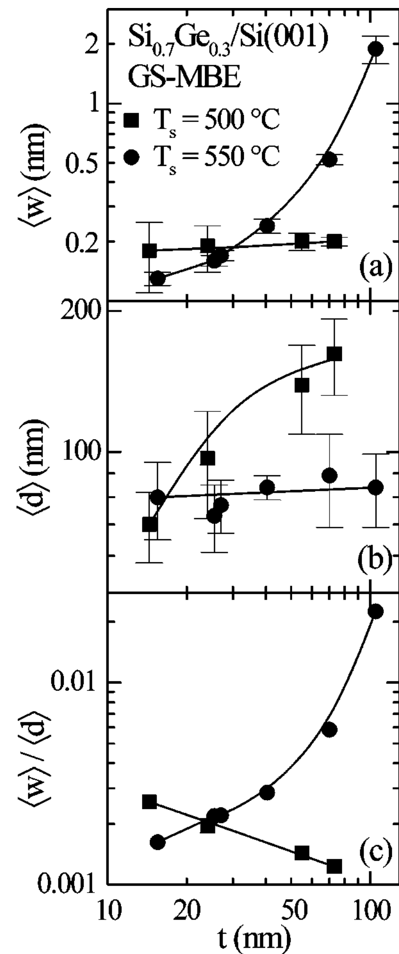

FIG. 6. Plots of the (a) surface width $\langle w \rangle$, (b) in-plane coherence length $\langle d \rangle$, and (c) aspect ratio $\langle w \rangle / \langle d \rangle$ as a function of film thickness for $Si_{0.7}Ge_{0.3}$ layers grown on Si(001) at $T_s=500$ and 550 °C.

nm [Fig. 6(b)]. Thus, the mounds display significant in-plane coarsening as the aspect ratio $\langle w \rangle / \langle d \rangle$ decreases by a factor of $\simeq 2.1$ [Fig. 6(c)], from 2.6×10^{-3} to 1.2×10^{-3}. The 2D slope histograms of these layers are slightly wider than those of the 450 °C samples. However, they still have a Gaussian intensity distribution with no intensity beyond 2.5°, consistent with the low aspect ratios of the mounds.

$Si_{0.7}Ge_{0.3}(001)$ layers deposited at 550 °C also exhibit the formation of small, compact, rounded growth mounds at an early stage of film growth as shown by the AFM image in Fig. 4(e) of a 27-nm-thick layer. A comparison with images of 500 °C layers having approximately the same thickness [see, for example, Fig. 4(c)], reveals that the 550 °C mounds are much better defined. A higher-resolution view of the $T_s=550\,°C$ mounds is shown in the $100\times100\ nm^2$ *in situ* STM image of a sample with $t=25$ nm [Fig 5(b)]. The mounds consist of approximately five to seven atomic layers, with the upper islands elongated along the ⟨110⟩ directions, compared to the single height islands obtained at $T_s=450\,°C$ [Fig. 5(a)].

Mound growth during $Si_{0.7}Ge_{0.3}(001)$ epitaxy at $T_s=550\,°C$ follows a quite different pathway than at lower temperatures. Figure 6 shows that at 550 °C, $\langle d \rangle$ remains approximately constant at $\simeq 85$ nm over the full range of layer thicknesses, up to 105 nm, whereas $\langle w \rangle$ increases by more than a factor of 10, from 0.13 nm at $t=15$ nm to 1.9 nm with $t=105$ nm. Thus, the mounds, which are initially similar to those at $T_s=500\,°C$, grow vertically, rather than laterally, resulting in their aspect ratio $\langle w \rangle / \langle d \rangle$ increasing from 1.6×10^{-3} to 22×10^{-3} across this thickness range. The fact that $\langle d \rangle$ remains constant as a function of t indicates a lack of significant mound coalescence.

For 550 °C layers with $t \leqslant 70$ nm, the 2D slope histograms are characterized by relatively narrow distributions centered at the origin and extending out to 4°, compared to 2.5° for layers grown at $T_s=500\,°C$. As the 550 °C $Si_{0.7}Ge_{0.3}(001)$ alloy layer thicknesses exceed $\simeq 70$ nm, however, the growth mounds evolve into self-organized pyramidal structures composed of rectangular-shaped bases with edges aligned along the elastically soft[22] ⟨100⟩ directions. At $t=105$ nm [Fig. 4(f)], the intensity is still highest at the origin, but now extends out along the four $\langle 10\ell \rangle$ directions up to $\simeq 11.3°$, the angle corresponding to {105} facets. Thus, the rounded growth mounds transform into pyramid-shaped structures. Line scans of the pyramids show that while their lower edges are bounded by {105} facets, the tops are still rounded.

Downloaded 07 Nov 2002 to 130.126.102.122. Redistribution subject to AIP license or copyright, see http://ojps.aip.org/japo/japcr.jsp

IV. DISCUSSION

The results presented in Sec. III show that increasing T_s from 450 to 500 to 550 °C produces strikingly different surface morphological evolution pathways during the growth of fully coherent $Si_{0.7}Ge_{0.3}$ layers on Si(001) by GS-MBE. Films grown at $T_s = 450$ °C remain flat and featureless with $\langle w \rangle < 0.15$ nm up to the critical thickness for misfit dislocations, $t_c \simeq 100$ nm. The surface morphology of layers grown at 500 °C consists of small compact rounded growth mounds with very low aspect ratios, $\langle w \rangle / \langle d \rangle < 2 \times 10^{-3}$, and no evidence of faceting. The 500 °C mounds increase in lateral size $\langle d \rangle$ from $\simeq 70$ to 162 nm as t is increased from 14 to 75 nm. However, $\langle w \rangle$ remains essentially constant at $\simeq 0.2$ nm, resulting in a decrease in the aspect ratio $\langle w \rangle / \langle d \rangle$ by a factor of $\simeq 2.1$. Layers deposited at 550 °C also exhibit growth mounds, but with better definition and in-plane self-organization. In distinct contrast to the 500 °C films, $\langle d \rangle$ for 550 °C layers remains constant at $\simeq 85$ nm as a function of film thickness ($t = 15$–105 nm), whereas $\langle w \rangle$ increases by more than a factor of 10, from 0.13 to 1.9 nm. The mounds develop {105} faceted sides at $t > 70$ nm.

The two primary mechanisms that control surface morphological evolution during epitaxial growth are kinetic and strain-induced roughening. The former is typically associated with low-temperature growth while the latter occurs at higher temperatures. Kinetic roughening[23–26] has been shown to be due to the presence of Ehrlich barriers, E_b, to the migration of adatoms over down steps and/or step-edge attraction.[27–30] This, in turn, leads to a divergence in adatom flux and, hence, increased nucleation on terraces that results in surface roughening, the amplitude of which increases with increasing in film thickness.

The fact that GS-MBE layers grown at 450 °C exhibit no measurable roughening with increasing layer thickness demonstrates that E_b has a negligible effect on adatom descending-step crossing probabilities at $T_s \geq 450$ °C. That is, kinetic roughening is already quenched at 450 °C and is therefore inconsequential at 500 and 550 °C. Thus, the surface roughening we observe at higher temperature must be driven by heteroepitaxial strain.

Jesson *et al.*[31] noted that strain-induced roughening during SS-MBE of compressively strained layers occurs as a result of spatial gradients in the surface chemical potential μ. They recognized that the gradients provide an adatom drift velocity and, following the work in Refs. 4 and 32, derived equations for the time evolution of the surface topographical profile during growth. The overall behavior is controlled by two primary competing terms. The first, which corresponds to the surface free energy contribution to the chemical potential, depends on the local curvature of the surface and tends to flatten the profile, while the second term is the elastic energy contribution which includes the square of the local stress tangential to the surface and gives rise to a net flux of adatoms from valleys toward peak regions.

Determining the point at which a flat strained-layer becomes unstable with respect to a periodic perturbation of small amplitude is equivalent to establishing the *onset* of strain-induced surface roughening. A simple one-dimensional analysis shows that the critical perturbation wavelength λ_c for initiating roughening is given by[33]

$$\lambda_c = \frac{\pi \gamma}{(1+\nu)\xi}. \tag{1}$$

γ in Eq. (1) is the surface energy per unit area and ξ is the strain energy per unit volume,

$$\xi = \frac{2G(1+\nu)\varepsilon^2}{(1-\nu)}, \tag{2}$$

in which G is the film shear modulus, ν is the Poisson ratio, and ε is the layer/substrate lattice constant mismatch. When $\lambda < \lambda_c$, the chemical potential μ is larger near the peak in the surface perturbation than in the trough and surface diffusion tends to smoothen the surface by transporting atoms from peaks to valleys. Conversely, μ is lower in the peak regions when $\lambda > \lambda_c$ and uphill surface diffusion from valleys to peaks results in amplification of the surface perturbation. Thus, λ_c sets an *intrinsic* length scale for surface roughening while elevated temperatures are required to drive the uphill diffusion process.

For $Si_{0.7}Ge_{0.3}(001)$, assuming a linear interpolation between Si and Ge: $\gamma = 1.32\ \mathrm{J\,m^{-2}}$,[34,35] $G = 4.78 \times 10^{10}\ \mathrm{N\,m^{-2}}$,[35] $\nu = 0.278$,[35] and $\varepsilon = 0.125$. Substituting these values into Eqs. (1) and (2) yields $\lambda_c \simeq 120$ nm, which is in reasonable agreement, given the simplifying assumptions inherent in deriving Eqs. (1) and (2), with our measured $\langle d \rangle$ values, $\simeq 70$ and 80 nm, at the smallest film thicknesses for layers grown at 500 and 550 °C, respectively. This suggests that strain-induced roughening determines the *initial* perturbation wavelength during $Si_{0.7}Ge_{0.3}(001)$ GS-MBE at both growth temperatures.

While the $T_s = 500$ and 550 °C samples exhibit strain-induced mound formation at the smallest layer thicknesses examined, the results in Sec. III show that for $Si_{0.7}Ge_{0.3}(001)$ GS-MBE at 450 °C, growth surfaces remain atomically smooth even for layer thicknesses up to critical values for dislocation nucleation. From this observation, we can draw two immediate conclusions. (1) Since we do not observe significant terrace nucleation leading to mound formation at 450 °C, the adatom mean free path L is of the order of the average terrace width which, for miscut of 0.1° along ⟨110⟩, is $\simeq 80$ nm. (2) The probability for adatoms to cross ascending steps at 450 °C is small. As will be discussed, even at $T_s = 500$ °C, where mound formation is first observed, the mounds grow laterally much faster than they roughen vertically indicating that ascending step-crossing probabilities are still low.

Based upon the above discussion, it is clear that the step-edge trap energy E_t must be much larger than E_b. This is certainly consistent with what little data are available. *Ab initio* local density functional and pseudopotential calculations predict activation energies of 0.85 and 1.0 eV for adatoms to cross ascending A and B steps, respectively, on Si(001).[36] (Comparable values do not exist for $Si_{1-x}Ge_x(001)$.) Based upon an experimentally determined adatom surface diffusion energy E_s on Si(001) of 0.67 eV,[37,38] and assuming, as discussed above that E_b is negligible, E_t is of the order of 0.2–0.3 eV. At the growth tem-

Downloaded 07 Nov 2002 to 130.126.102.122. Redistribution subject to AIP license or copyright, see http://ojps.aip.org/japo/japcr.jsp

peratures used in the present experiments, it is believed that the primary diffusing species on Si(001),[39] and hence $Si_{1-x}Ge_x(001)$,[40] are dimers. The activation energy for diffusion of a Si ad-dimer along Si(001) dimer rows has been measured and calculated to be $\simeq 1.1$ eV.[39] Using the experimentally determined activation energy for ad-dimer formation from kink sites at Si(001) steps,[41,42] $E_t + E_s \simeq 1.45$ eV, we estimate that E_t is of the order of 0.3–0.4 eV for Si ad-dimers.

The high rate of roughening we observe at $T_s = 550\,°C$, with $\langle w \rangle$ increasing by almost a factor of 15 as t is increased from 15 to 105 nm, indicates that mass transport over ascending step edges occurs with high probability at this growth temperature. Using covalent radii and assuming spherical mounds at 500 °C and pyramidal mounds at 550 °C, we calculate from our AFM results that the fraction of mound atoms residing in upper layers (above the bottom layer) is $\simeq 83\%$ for the thickest film at 550 °C compared to only 3% at 500 °C. This is a very dramatic change over a relatively narrow growth temperature range and we propose, as discussed below, that the large decrease in ascending step-crossing probabilities as T_s is reduced from 550 to 500 °C results not just from corresponding differences in thermal activation, but also from large T_s-induced variations in hydrogen step-edge coverages as well.

A. Mean surface diffusion lengths

Two-dimensional growth requires significant adatom diffusion lengths which generally imply relatively high temperatures since surface diffusion is thermally activated. However, film growth by GS-MBE (as opposed to by SS-MBE) has the interesting characteristic that mean diffusion lengths can actually increase at lower temperatures due to higher steady-state coverage of product species (in this case, hydrogen). Increasing H coverages θ_H not only affects surface diffusion lengths directly, but indirectly as well through significant changes in film growth rates R, even at constant precursor flux.

From universal scaling theory[43] and experimental observations[38,44–46] during film growth, L is related to the surface diffusivity D_s and the deposition rate R through the expression

$$L \propto \left(\frac{D_s}{R} \right)^{\alpha}, \tag{3}$$

where the exponent α depends upon the critical nucleus size and ranges from 1/6 to 1/2. Whereas L in SS-MBE, in which R is independent of T_s for normal growth conditions, decreases with decreasing T_s as a result of the exponential dependence of D_s on T_s, it is clear from the above discussion that L in GS-MBE can either decrease *or* increase at lower T_s depending on the relative activation energies of D_s and R.

Using STM results, Vasek *et al.*[47] have determined that small θ_H values increase the activation energy E_s of Si adatom motion on Si(001) terraces at $T_s \lesssim 250\,°C$. At higher T_s, however, surface H atoms are sufficiently mobile that they have little effect on Si adatom diffusion and E_s remains close to the value observed for clean Si(001). We expect similar results for ad-dimer diffusion. Since all growth experiments in this study were carried out at $T_s \geqslant 450\,°C$, the effect of θ_H on Si terrace diffusivity should be negligible.

However, while D_s in Eq. (3) does not depend strongly on θ_H during GS-MBE, R does. The film growth rate varies as the square of the dangling bond coverage θ_{db} through the expression,[15]

$$R = \frac{2SJ\theta_{db}^2}{N}, \tag{4}$$

where $\theta_{db} = (1-\theta_H)$, J is the incident precursor flux, S is the average precursor reactive sticking probability, and N is the bulk $Si_{0.7}Ge_{0.3}$ atom number density, 4.8×10^{22} cm^{-3}. Based upon second-order H_2 desorption kinetics from the $Si_{1-x}Ge_x(001)$ surface, θ_{db} can be expressed as[13,15]

$$\theta_{db} = \left(1 + \sqrt{\frac{2JS}{N_s \nu_s \exp(-E_d/kT_s)}} \right)^{-1}. \tag{5}$$

N_s in Eq. (5) is the surface atom density, 6.8×10^{14} cm^{-2}, ν_s is the attempt frequency, and E_d is the activation energy for H_2 desorption. We have written Eqs. (4) and (5) for average values of S, ν_s, and E_d since θ_{Ge} remains approximately constant over the T_s range of these experiments (Table I) and S depends only weakly on T_s.[15,48,49] Thus, R depends primarily on E_d through the term θ_{db}^2.

The H_2 desorption energy during GS-MBE growth of $Si_{0.7}Ge_{0.3}(001)$ ($E_d = 2.0$ eV)[13,15,18] is significantly higher than the surface diffusion energy for Si adatoms ($E_s = 0.67$ eV),[37] Si ad-dimers ($E_s = 1.1$ eV),[39] and SiGe mixed ad-dimers ($E_s = 1.0$ eV) (Ref. 40) on Si(001). Corresponding values for Ge adatoms and ad-dimers on Ge-rich $Si_{1-x}Ge_x(001)$ (Ref. 38) surfaces are expected to be even lower. This can give rise to the counterintuitive result of larger L values at lower T_s. Using activation energies of surface diffusion varying from 0.7 to 1.1 eV, we calculate that D_s values decrease by a factor of 2–3 with a decrease in T_s from 550 to 500 °C. As shown in Table I, R decreases by a factor of $\simeq 2$ between 550 and 500 °C leading, through Eq. (3), to a similar L value at these temperatures. In contrast, the decrease in D_s from 500 to 450 °C is more than overcome by the much larger decrease in $R(\simeq 7.5\times)$. Thus, in the present experiments, L is larger at $T_s = 450\,°C$ than at 500 and 550 °C. This is consistent with our AFM and STM results showing 2D growth with atomically flat surfaces and large terraces at low T_s (450 °C), and the formation of growth mounds at higher T_s (500–550 °C).

B. Ascending step crossing

While surface H appears to have little effect on adatom mobilities during $Si_{1-x}Ge_x(001)$ GS-MBE, H atoms at step edges can significantly affect adatom ascending step-crossing probabilities. First-principles total-energy calculations have shown that the presence of H at a step edge increases E_t for adatoms by $\simeq 0.1$ and 0.8 eV at S_A and S_B steps, respectively.[50] Thus, we expect that the higher steady-state H surface coverages obtained at lower growth temperatures in our experiments will lead to decreased mass transport across ascending steps. Two-dimensional surface segregation of H

Downloaded 07 Nov 2002 to 130.126.102.122. Redistribution subject to AIP license or copyright, see http://ojps.aip.org/japo/japcr.jsp

toward step edges, for which there is some experimental evidence,[51] would serve to amplify this effect.

Since L remains approximately constant during GS-MBE $Si_{1-x}Ge_x(001)$ at 500 and 550 °C, the large differences we observe in surface morphological evolution at these two temperatures must be due to increased ascending step crossing resulting from both lower H coverages and higher thermal activation. Increasing T_s from 500 to 550 °C decreases θ_H by a factor of 2.4 from 0.26 to 0.11 ML, thereby enhancing the ascending step-crossing rates, leading to shorter nucleation lengths on upper terraces and, hence, rapid roughening. Since both the upward and downward step-crossing currents are large in this case, the mounds are continuously exchanging adatoms at high rates and the roughening we observe occurs in response to the heteroepitaxial strain driving force.

At $T_s = 500$ °C, surface mounds experience rapid lateral growth and $\langle d \rangle$ increases from 70 nm at $t = 14$ nm to 162 nm at $t = 75$ nm due to step edges acting as effective adatom sinks, with $\langle w \rangle$ remaining approximately constant at $\simeq 0.2$ nm. In the absence of significant mass transport over ascending steps at 500 °C, the probability of nucleating a new layer remains small until the lateral size of the upper islands becomes of the order of $2L$.

The mounds formed at $T_s = 550$ °C transform into {105} faceted pyramids at $t > 70$ nm due to repulsive step–step interactions which limit the facet angle.[52,53] The lateral mound size remains constant, thus vertical growth results in an increase in the average sidewall angle and a corresponding decrease in the average terrace step separation. Repulsive step–step interactions[52] lead to maximum sidewall angles of 11.3° as viewed along ⟨100⟩ directions, i.e., a pyramid bounded by {105} facets.

V. CONCLUSIONS

We have shown that the presence of hydrogen at the growth surface can play a major role in controlling surface morphological evolution during deposition of fully coherent, compressively strained heteroepitaxial semiconductor layers. Specifically, we found that increasing the steady-state hydrogen coverages θ_H, through a decrease in T_s, during $Si_{0.7}Ge_{0.3}/Si(001)$ GS-MBE from Ge_2H_6/Si_2H_6 mixtures quenches strain-induced surface roughening at growth temperatures for which it is observed during SS-MBE.

The large differences in GS-MBE $Si_{1-x}Ge_x/Si(001)$ surface morphological evolution that occurs over a relatively narrow growth temperature range (450–550 °C) are due primarily to T_s-dependent effects of θ_H on film growth rates R, surface diffusion rates D_s, and ascending step-crossing probabilities. $Si_{0.7}Ge_{0.3}(001)$ layers grown at $T_s = 450$ °C, where $\theta_H = 0.52$ ML, remain two dimensional over the entire film thickness range investigated (up to the point at which misfit dislocation formation occurs) since both R and the probability of crossing ascending steps are low. Raising T_s to 500 °C ($\theta_H = 0.26$ ML) increases R faster than D_s, leading to shorter mean surface diffusion lengths and resulting in the formation of growth mounds. However, the steady-state hydrogen coverage at $T_s = 500$ °C is sufficient to maintain the ascending step-crossing probability relatively small such that the mounds spread laterally due to preferential adatom attachment at mound edges, with very little gain in height. At $T_s = 550$ °C, the ascending step-crossing probability increases due to both higher thermal activation and lower hydrogen coverages ($\theta_H = 0.11$ ML), leading, under the strain driving force, to the formation of 3D faceted pyramids similar to those observed during SS-MBE. With continued film growth, the pyramids rapidly increase in height whereas the in-plane coherence length remains approximately constant.

ACKNOWLEDGMENTS

The authors gratefully acknowledge the financial support of the U.S. Department of Energy, Division of Materials Sciences, under Contract No. DEFG02-ER9645439 and of the NSF Focused Research Group on Nanoscale Morphological Control of Strained Semiconductor Surfaces, Grant No. DMR-0075116, during the course of this research. One the authors (P.D.) was partially supported by the Natural Sciences and Engineering Research Council (NSERC) of Canada and by the Fonds pour la Formation de Chercheurs et l'Aide à la Recherche (FCAR), Québec, Canada.

[1] Q. Lu, M. R. Sardela, Jr., T. R. Bramblett, and J. E. Greene, J. Appl. Phys. **80**, 4458 (1996).
[2] G. Abstreiter, H. Brugger, T. Wolf, H. Jorke, and H. J. Herzog, Phys. Rev. Lett. **54**, 2441 (1985).
[3] P. M. Petroff and G. Medeiros-Ribeiro, MRS Bull. **21**, 50 (1996).
[4] D. J. Srolovitz, Acta Metall. **37**, 621 (1989).
[5] J. Tersoff and F. K. LeGoues, Phys. Rev. Lett. **72**, 3570 (1994).
[6] N. E. Lee, M. Matsuoka, M. R. Sardela, Jr., F. Tian, and J. E. Greene, J. Appl. Phys. **80**, 812 (1996).
[7] B. Gallas, I. Berbezier, A. Ronda, and J. Derrien, Thin Solid Films **294**, 22 (1997).
[8] I. Berbezier, B. Gallas, A. Ronda, and J. Derrien, Surf. Sci. **412–413**, 415 (1998).
[9] N. E. Lee, D. G. Cahill, and J. E. Greene, J. Appl. Phys. **80**, 2199 (1996).
[10] H. Hirayama, T. Tatsumi, and N. Aizaki, J. Cryst. Growth **95**, 476 (1989).
[11] H. Hirayama, M. Hiroi, K. Koyama, and T. Tatsumi, Appl. Phys. Lett. **56**, 1107 (1990).
[12] S. Bozzo *et al.*, J. Cryst. Growth **216**, 171 (2000).
[13] H. Kim, N. Taylor, J. R. Abelson, and J. E. Greene, J. Appl. Phys. **82**, 6062 (1997).
[14] Q. Lu, T. R. Bramblett, N. E. Lee, M. A. Hasan, T. Karasawa, and J. E. Greene, J. Appl. Phys. **77**, 3067 (1995).
[15] H. Kim, N. Taylor, T. R. Bramblett, and J. E. Greene, J. Appl. Phys. **84**, 6372 (1998).
[16] L. R. Doolittle, Nucl. Instrum. Methods Phys. Res. B **9**, 344 (1985).
[17] L. G. Parratt, Phys. Rev. **95**, 359 (1954).
[18] H. Kim, P. Desjardins, J. R. Abelson, and J. E. Greene, Phys. Rev. B **58**, 4803 (1998).
[19] E. Chason and T. M. Mayer, CRC Crit. Rev. Solid State Mater. Sci. **22**, 1 (1997).
[20] S. Takagi, Acta Crystallogr. **15**, 1311 (1962).
[21] D. Taupin, Bull. Soc. Fr. Mineral. Cristallogr. **87**, 469 (1964).
[22] V. A. Shchukin, N. N. Ledentsov, P. S. Kopev, and D. Bimberg, Phys. Rev. Lett. **75**, 2968 (1995).
[23] J. E. Van Nostrand, S. J. Chey, M. A. Hasan, D. G. Cahill, and J. E. Greene, Phys. Rev. Lett. **74**, 1127 (1995).
[24] J. E. Van Nostrand, S. Jay Chey, and D. G. Cahill, Phys. Rev. B **57**, 12536 (1998).
[25] N. E. Lee, D. G. Cahill, and J. E. Greene, Phys. Rev. B **53**, 7876 (1996).
[26] B. W. Karr, I. Petrov, P. Desjardins, D. G. Cahill, and J. E. Greene, Surf. Coat. Technol. **94–95**, 403 (1997).
[27] S. C. Wang and G. Ehrlich, Phys. Rev. Lett. **70**, 41 (1993).
[28] S. C. Wang and G. Ehrlich, Phys. Rev. Lett. **71**, 4174 (1993).
[29] G. Ehrlich, Surf. Sci. **331–333**, 865 (1995).
[30] A. Golzhauser and G. Ehrlich, Phys. Rev. Lett. **77**, 1334 (1996).

Downloaded 07 Nov 2002 to 130.126.102.122. Redistribution subject to AIP license or copyright, see http://ojps.aip.org/japo/japcr.jsp

[31] D. E. Jesson, S. J. Pennycook, J. M. Baribeau, and D. C. Houghton, Phys. Rev. Lett. **71**, 1744 (1993).
[32] W. W. Mullins, J. Appl. Phys. **28**, 333 (1957).
[33] H. Gao, J. Mech. Phys. Solids **42**, 741 (1994).
[34] D. J. Eaglesham, A. E. White, L. C. Feldman, N. Moriya, and D. C. Jacobson, Phys. Rev. Lett. **70**, 1643 (1993).
[35] K.-N. Tu, J. W. Mayer, and L. C. Feldman, *Electronic Thin Film Science for Electrical Engineers and Materials Scientists* (Macmillan, New York, 1992), Appendix E.
[36] Q.-M. Zhang, C. Roland, P. Boguslawski, and J. Bernholc, Phys. Rev. Lett. **75**, 101 (1995).
[37] Y. W. Mo, J. Kleiner, M. B. Webb, and M. G. Lagally, Phys. Rev. Lett. **66**, 1998 (1991).
[38] Y. W. Mo, J. Kleiner, M. B. Webb, and M. G. Lagally, Surf. Sci. **268**, 275 (1992).
[39] M. Krueger, B. Borovsky, and E. Ganz, Surf. Sci. **385**, 146 (1997).
[40] X. R. Qin, B. S. Swartzentruber, and M. G. Lagally, Phys. Rev. Lett. **85**, 3660 (2000).
[41] N. C. Bartelt, W. Theis, and R. M. Tromp, Phys. Rev. B **54**, 11741 (1996).
[42] N. C. Bartelt and R. M. Tromp, Phys. Rev. B **54**, 11731 (1996).
[43] A. Pimpinelli and J. Villain, *Physics of Crystal Growth* (Cambridge University Press, Cambridge, UK, 1998), p. 181.
[44] J. A. Stroscio, D. T. Pierce, and R. A. Dragoset, Phys. Rev. Lett. **70**, 3615 (1993).
[45] J.-P. Bucher, E. Hahn, P. Fernandez, C. Massobrio, and K. Kern, Europhys. Lett. **27**, 473 (1994).
[46] I. K. Robinson, K. L. Whiteaker, and D. A. Walko, Physica B **221**, 70 (1996).
[47] J. E. Vasek, Z. Zhang, C. T. Salling, and M. G. Lagally, Phys. Rev. B **51**, 17207 (1995).
[48] T. R. Bramblett, Q. Lu, T. Karasawa, M. A. Hasan, S. K. Jo, and J. E. Greene, J. Appl. Phys. **76**, 1884 (1994).
[49] T. R. Bramblett, Q. Lu, N. E. Lee, N. Taylor, M. A. Hasan, and J. E. Greene, J. Appl. Phys. **77**, 1504 (1995).
[50] S. Jeong and A. Oshiyama, Phys. Rev. Lett. **81**, 5366 (1998).
[51] J. Zhang, A. K. Lees, A. G. Taylor, M. H. Xie, B. A. Joyce, Z. Sobiesierksi, and D. I. Westwood, J. Cryst. Growth **175–176**, 477 (1997).
[52] K. M. Chen, D. E. Jesson, S. J. Pennycook, T. Thundat, and R. J. Warmack, Phys. Rev. B **56**, R1700 (1997).
[53] H. Ibach, Surf. Sci. Rep. **29**, 193 (1997).

Downloaded 07 Nov 2002 to 130.126.102.122. Redistribution subject to AIP license or copyright, see http://ojps.aip.org/japo/japcr.jsp